ACS Energy LETTERS

http://pubs.acs.org/journal/aelccp

Unveiling the Local Structure and the Ligand Field of Organic Cation Preintercalated Vanadate Cathode for Aqueous Zinc-Ion Batteries

Heng Liu, Huanhuan Niu, Wei-Hsiang Huang, Ting Shen, Changyuan Li, Chun-Chi Chang, Menghao Yang, Chenlong Gao, Long Yang, Quan Zong, Yanzhong Pei, Guozhong Cao,* and Chaofeng Liu*

Cite This: *ACS Energy Lett.* 2024, 9, 5492−5501

ABSTRACT: Layered vanadium-based materials have been extensively studied as promising cathode materials for aqueous zinc-ion batteries (AZIBs). However, challenges remain to achieve the desired high energy conversion efficiency and energy densities as well as long cycling stability requiring an in-depth understanding of the local and the electronic structure of a vanadium-based cathode, especially concerning the impacts on electrochemical potential and mass transfer in the electrochemical process. In this work, 1-butyl-1-methylpyrrolidinium cations are preintercalated into the layered hydrate vanadium pentoxide ($V_2O_5{\cdot}nH_2O$) and partially replace the electroneutral structural water, changing the local atomic environment. X-ray absorption spectroscopies demonstrate the V−O bond elongation and the distortion in the [VO_6] octahedra, which alter the ligand field and brings the V 3*d* state to a lower energy level, ultimately leading to an increase in the electrochemical potential. It is also revealed that the preintercalated organic cations exert electrostatic interaction with lattice oxygen, stabilizing the layered structure and buffering lattice strain during cycling. Consequently, the modified cathode achieves a superior specific capacity of 412 mAh/g at 0.5 A/g and a capacity retention of 97% after 3000 cycles at 8 A/g. The unveiled correlation between local structure and electrochemical performance paves the way for optimizing the cathode materials by manipulating the local coordination environment.

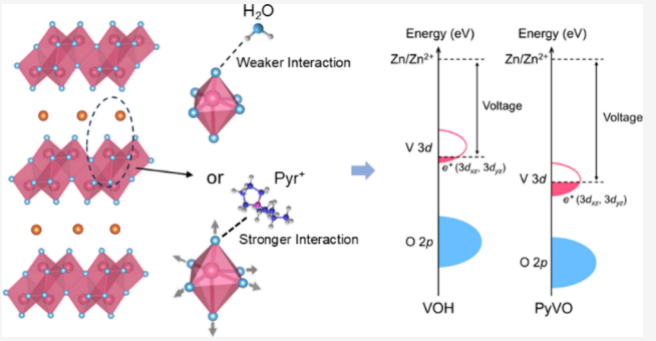

Presently, lithium-ion batteries (LIBs) stand as the predominant power sources for smart devices and electric vehicles due to their commendable attributes such as high energy density, affordability, and satisfactory lifespan.[1] However, LIBs fall short of meeting the increasingly stringent criteria for environmental sustainability and high safety in large-scale energy storage applications. As a result, both the academic and industrial communities are actively engaged in the pursuit of safer, more efficient electrochemical energy storage systems. Aqueous zinc-ion batteries (AZIBs) have garnered widespread attention,[2] partly owing to the favorable characteristics of the zinc metal anode. Zinc metal exhibits a high theoretical capacity of 820 mAh/g or 5851 mAh/cm^3, a relatively low redox potential (−0.76 V versus SHE), and a cost merely one-eighth of lithium's.[3] However, the development of AZIBs is constrained by the lack of suitable cathode materials. Manganese oxides,[4,5] Prussian blue and its analogues,[6−8] organics,[9,10] and vanadium oxides[11,12] have been extensively investigated as potential cathodes for AZIBs. Among them, vanadium oxides offer a notably higher theoretical capacity over 580 mAh/g owing to the variable chemical valences of vanadium ranging from +5 to +3.[13] Additionally, the open tunneled/layered structure of vanadium oxides cathodes can facilitate the diffusion of Zn^{2+}, beneficial to the rate performance.[14−16] Nevertheless, similar to all cathode

Received: October 1, 2024
Accepted: October 18, 2024

https://doi.org/10.1021/acsenergylett.4c02709
ACS Energy Lett. 2024, 9, 5492−5501

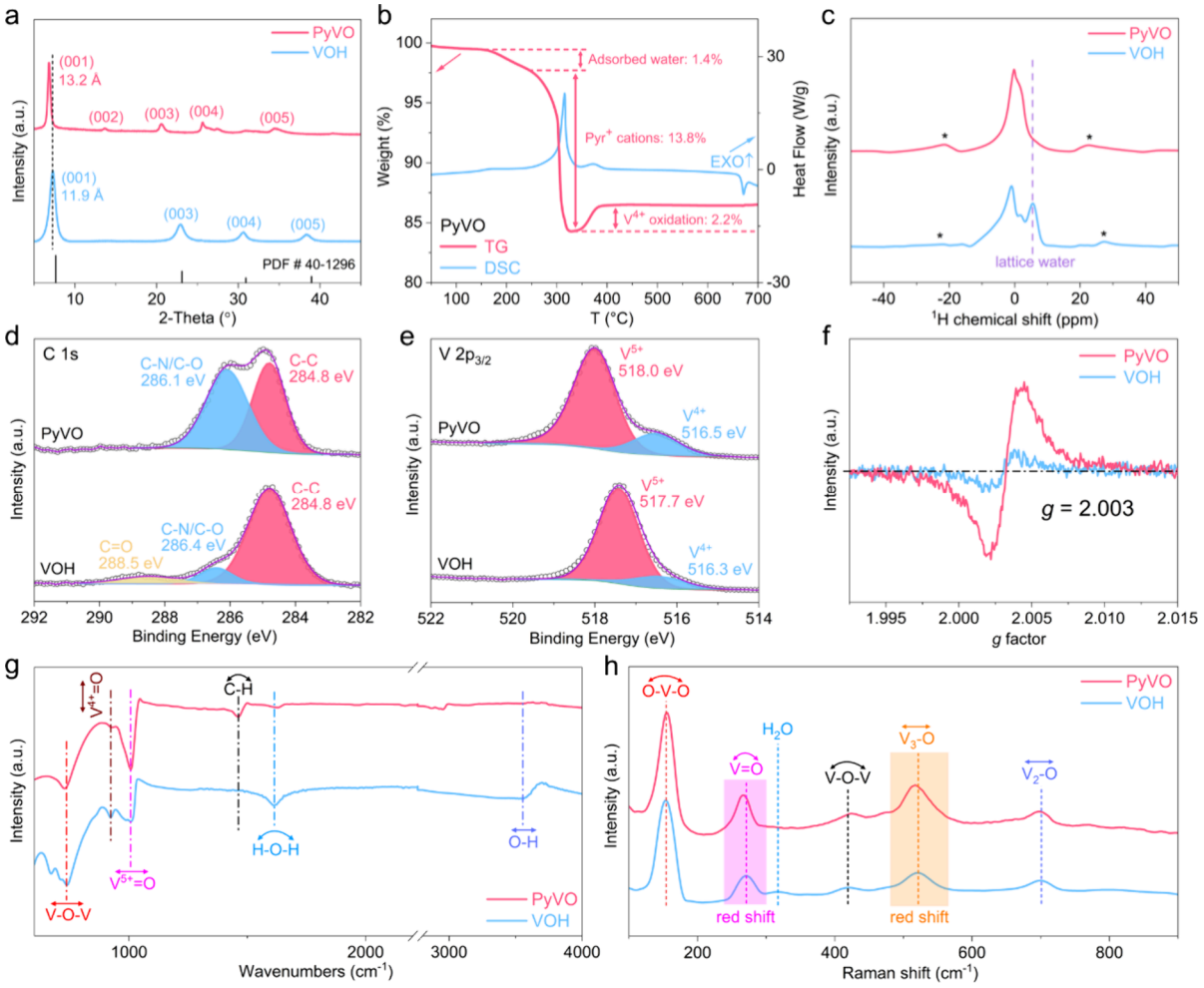

Figure 1. Structural, composition, chemical states, and bonding information on PyVO and VOH. (a) XRD patterns. The lattice spacing of (001) is expanded from 11.9 to 13.2 Å after the intercalation of Pyr^+. (b) TG/DSC curves of PyVO. The weight loss occurring at 250−350 °C originates from the removal of Pyr^+ from the lattice. (c) Solid-state ^1H NMR spectra of PyVO and VOH. The absence of lattice water signal in PyVO suggests that the insertion of Pyr^+ leads to the removal of lattice water. High-resolution XPS spectra of (d) C 1s and (e) V $2p_{3/2}$. The ratio of $V^{4+}/(V^{4+} + V^{5+})$ is higher in PyVO. (f) EPR spectra. PyVO exhibits a much stronger symmetric peak with a *g* value of 2.003, further verifying the increased proportion of V^{4+} in PyVO. (g) FTIR spectra. The presence of the peak assigned to the stretching vibration of C−H in PyVO indicates the successful introduction of Pyr^+ between the layers. (h) Raman spectra. The red shifts observed in the peaks of the V=O bonds and V_3−O bonds suggest longer bond lengths in PyVO.

materials for zinc ion intercalation, strong electrostatic interaction between anion sublattice and divalent zinc ions in vanadium oxides leads to slow diffusion, low capacity, and relatively quick capacity decay.

Hydrate vanadium pentoxide ($V_2O_5{\cdot}nH_2O$, VOH), as a representative of vanadium-based materials, has a layered structure. The interlayer lattice water expands the layer spacing and functions as "lubricant" to alleviate the electrostatic interaction between Zn^{2+} and the lattice, facilitating the fast diffusion of Zn^{2+}.[15,17] However, the weak interaction, van der Waals force connects the interlayers, which could not accommodate the lattice strain and causes the structure deterioration in the ion insertion/extraction process, threatening the practical application of VOH.[18,19] To address this challenge, prior studies have preintercalated inorganic ions, such as Li^+, NH_4^+, Mn^{2+}, Ni^{2+}, and Al^{3+},[14,20−24] between [VO] layers, to ulteriorly stabilize the layer structure through forming robust bonds with the V−O framework.[25] Efforts have also been made to explore the incorporation of organic molecules and polymers as intercalants, such as ethylene glycol (EG) molecules and polyaniline (PNAI) chains.[26,27] The flexibility of organics allows them to buffer the interlayer lattice strain, suppressing structure deterioration.[28] In addition, the organics with conjugated structure can shield the electrostatic interactions between Zn^{2+} and the [VO] framework, promoting fast Zn^{2+} diffusion.[19] Recently, investigations into organic cations have been undertaken.[18,29,30] Integrating the properties of inorganic ions and electroneutral organic compounds, the introduced organic cations have synthetic functions of expanding interlayer spacing, shielding the charge of Zn^{2+}, forming rigid electrostatic binding with [VO] skeleton, and buffering lattice strain during charging/discharging.[18,29] Considering these factors, organic cation preintercalation turns out to be an intriguing way to resolve the bottleneck that hinders the further development of hydrate vanadium pentoxide. However, the influences of the intercalants on the local and electrical structures of hydrate vanadium pentoxide remain ambiguous, particularly their roles in electrochemical potential, structural stability, and ion diffusion. This neces-

https://doi.org/10.1021/acsenergylett.4c02709
ACS Energy Lett. 2024, 9, 5492−5501

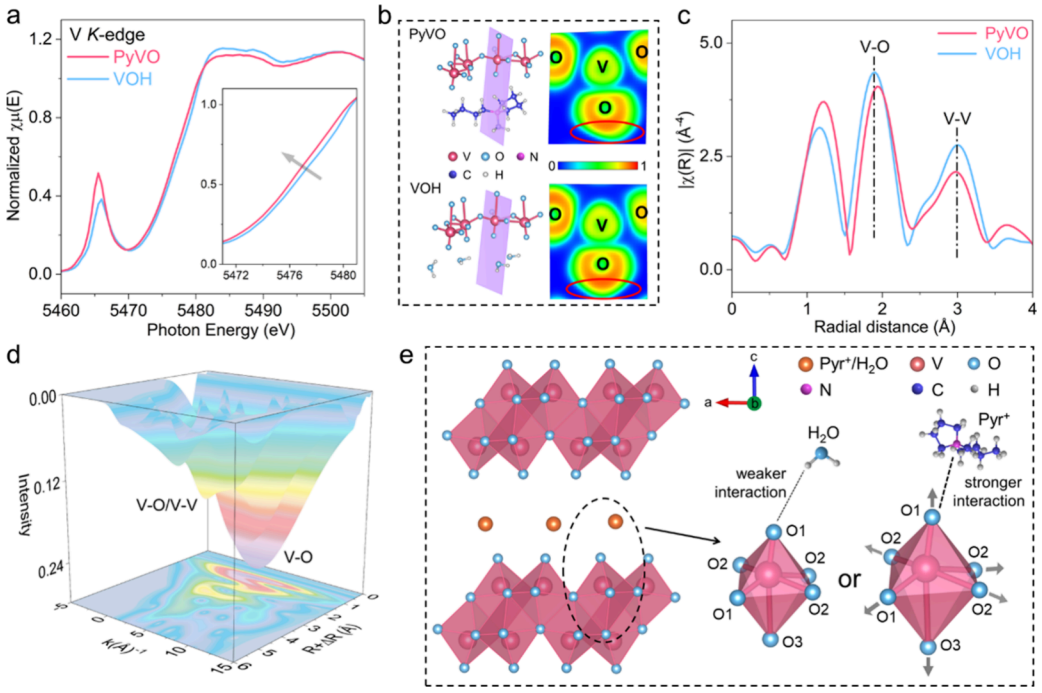

Figure 2. Local structure information on PyVO and VOH. (a) V *K*-edge XANES spectra. Stronger intensity of the pre-edge peak for PyVO suggests higher distorted polyhedra in PyVO. (b) The electron localization function (ELF) sections of both samples. The electropositive Pyr^+ can withdraw the electron from lattice oxygen, especially for the apical oxygen which is closer to Pyr^+, as emphasized by the red rings. (c) k^3-weighted Fourier transform of the V *K*-edge EXAFS. For PyVO, peaks assigned to V−O interatomic distance shift right compared with VOH, indicating longer V−O bonds in PyVO. (d) 3D wavelet transforms of PyVO. (e) Schematic illustration of the local structures. The stronger interaction exists between Pyr^+ and lattice oxygen. PyVO exhibits a higher degree of polyhedra distortion due to its higher ratio of V^{4+}.

sitates an in-depth investigation to address these issues and to fully utilize their potential.

In this study, organic cations (1-butyl-1-methylpyrrolidinium, $C_9H_{20}N^+$, denoted as Pyr^+) are preintercalated into the interlamination of hydrate vanadium pentoxide and replace the electroneutral interlayer lattice water. The variations in the local structure and the ligand field induced by this preintercalation are unveiled by X-ray adsorption chemistry. Our findings reveal that the intercalation of Pyr^+ cations results in the partial reduction of V^{5+} to V^{4+} that has a larger ion radius, causing the increase of the V−O bond length and the distortion of [VO_6] octahedra. Such distortion in the local V−O coordination environment decreases the energy level of the e^* ($3d_{yz}$, $3d_{xz}$) state, which is partly occupied by the 3*d* electron of V^{4+} ($3d^1$) and determines the electrochemical potential of the cathode. This change results in the higher electrochemical potential of the organic cation introduced cathode (PyVO), in comparison with VOH. In addition, the density functional theory (DFT) calculations imply that the introduced Pyr^+ expands the interlayer spacing and electrostatically connects with [VO] layers, leading to fast Zn^{2+} diffusion and strengthened layer structure. Owing to these modifications, the PyVO cathode delivers a specific capacity of 412 mAh/g at 0.5 A/g and a capacity retention of 97% after 3000 cycles at 8 A/g. The deciphered correlations between local structure and electrochemical performance provide fundamental guidance for designing next-generation, high-power-density batteries through the modulation of the local structure of cathode materials.

The XRD patterns of VOH and PyVO in Figure 1a are well indexed to $V_2O_5{\cdot}nH_2O$ (PDF 40-1296),[29] indicating PyVO and VOH have a similar [VO] bilayer structure, characterized by edge and corner sharing [VO_6] octahedra.[20] In PyVO, the (002) and (11$\bar{3}$) peaks arise at ∼13.5° and ∼27°, respectively, which is probably caused by the slight slipping of the [VO] slab.[31,32] The strongest peak at 6.82° corresponds to the (001) plane of PyVO, indicating an expanded interlayer spacing of 13.2 Å in contrast to 11.9 Å of VOH. Figure 1b presents the TG/DSC curves of PyVO. The weight loss of 1.4% occurs between 150 and 250 °C, accompanied by a weak exothermic peak, suggesting the removal of adsorbed water. The mass ratio of Pyr^+ can be determined as 13.8% by the weight loss occurring from 250 to 350 °C, coupled with a strong exothermic peak. A weight increase of 2.2% observed from 350 to 400 °C is attributed to the oxidation of V^{4+}, accompanied by oxygen incorporation. The endothermic peak at 670 °C marks the melting of V_2O_5.[20] The chemical formula of PyVO is estimated to be $[(C_9H_{20}N)_{0.2}]V_2O_5$. Similarly, from the data in Figure S1, the formula for VOH is determined as $V_2O_5{\cdot}1.1H_2O$. Therefore, most lattice water molecules between [V−O] layers are replaced by Pyr^+. Figure 1c displays the solid-state ^1H nuclear magnetic resonance (NMR) spectra of both samples. The spinning sidebands located at around ±22 ppm are marked by star symbols.[17] The peak at ∼5.4 ppm can be ascribed to lattice water.[17] Lattice water signal is not detected in PyVO, further validating its replacement by lattice water. Additionally, the high-resolution transmission electron microscopy (HRTEM) image in Figure S2 confirms the lattice fringes with a spacing of 13.2 Å, which is consistent with the XRD results. HRTEM-EDS mapping (Figure S3) verifies the homogeneous element distributions of V, O, C, and N elements in PyVO nanowires. No signal comes

https://doi.org/10.1021/acsenergylett.4c02709
ACS Energy Lett. 2024, 9, 5492−5501

from chlorine that is present in the precursor, suggesting the intercalation of Pyr^+ without anions.

X-ray photoelectron spectroscopy (XPS) of C 1*s* for both samples in Figure 1d reveal two peaks at approximately 284.8 and 286.4 eV, corresponding to C−C and C−N/C−O bonds from organics.[33,34] Notably, PyVO displays a significantly higher peak intensity for C−N/C−O, suggesting a greater quantity of organic components in PyVO. This finding provides supporting evidence for the intercalation of Pyr^+, corroborated by the N 1*s* spectra depicted in Figure S4, aligning with the Pyr^+ spectra reported in Mg ion batteries.[35] In Figure 1e, the XPS spectra of V $2p_{3/2}$ for PyVO exhibit two distinctive peaks, corresponding to V^{5+} and V^{4+} at 518.0 and 516.5 eV, respectively.[29,33] These peaks slightly shift toward higher binding energy compared to VOH, which can be ascribed to the replacement of lattice water by Pyr^+ cations, altering the coordination environment and the crystal field of vanadium. These spectra also indicate that the ratio of $V^{4+}/(V^{4+} + V^{5+})$ increases to 16.2% for PyVO in comparison to 9.0% of VOH. This change can be attributed to the insertion of Pyr^+ carrying positive charges. To maintain electrical neutrality, V^{5+} tends to accept electrons and undergo reduction to V^{4+}. A higher ratio of V^{4+}, which has a single electron in the 3*d* orbital, can enhance the electrical conductivity of PyVO.[20] The electron paramagnetic resonance (EPR) signal in Figure 1f comes from the magnetic moment of unpaired electrons.[36] The 3*d* orbital of V^{4+} has one unpaired electron, but V^{5+} is empty. Therefore, PyVO exhibits a stronger symmetric peak with a *g* value of 2.003, demonstrating an increased ratio of V^{4+} in PyVO. Fourier transform infrared spectroscopy (FT-IR) spectra are presented in Figure 1g. The peak located at 728 cm^{-1} corresponds to the antisymmetric V−O−V stretching vibration.[37] The peaks at 919 and 1010 cm^{-1} relate to the stretching vibration of V^{4+}=O and V^{5+}=O, respectively.[15] The peak at 1461 cm^{-1}, attributed to the C−H bending vibration,[27] is only observed in PyVO, indicating the intercalation of Pyr^+ as verified by XPS spectra. The peaks at 1613 and 3553 cm^{-1} correspond to the bending and stretching vibrations of O−H bonds in water molecules.[15,29] These two peaks associated with H_2O molecules are both nearly undetected in PyVO compared to VOH. Raman spectra in Figure 1h show that the peaks at 153 and 420 cm^{-1} originate from the bending vibration of O−V−O and V−O−V, respectively.[15,38] The peak at 701 cm^{-1} is indicative of the stretching vibrations within V_2−O bonds.[20] The peak at 317 cm^{-1} is from H_2O molecules, which is absent in PyVO.[29] Significantly, the peaks of PyVO assigned to the bending vibration of V=O at 271 cm^{-1} and the stretching vibration of V_3−O at 521 cm^{-1} show red shifts of 4.4 and 4.1 cm^{-1}, respectively, when compared to VOH.[39] The shifts suggest a weakening of the V=O and V_3−O bonds, accompanied by an increase in their respective lengths.[39]

Figure 2a shows the normalized V *K*-edge X-ray absorption near edge structure (XANES) spectra. Compared with VOH, the absorption edge and the pre-edge peak of PyVO both shift to lower energy, further confirming the lower valence state of vanadium in PyVO.[40] The intensity of the pre-edge peak corresponding to the electron transition from V 1*s* to V 3*d*-states provides information on the crystal field symmetry around vanadium and the distortion of V−O polyhedra.[41] This increased peak strength in PyVO is indicative of a substantial deformation or asymmetry within the polyhedral coordination environment.[42] The electron localization function (ELF) is obtained via density functional theory (DFT) calculations. The ELF sections of both samples are shown in Figure 2b. The electropositive Pyr^+ draws electrons of oxygen atoms toward themselves, especially from the oxygen that is closer to Pyr^+ at the octahedral vertex, suggesting the electrostatic interaction exists between Pyr^+ and lattice oxygen. Compared with the hydrogen bond in VOH, Pyr^+ imposes stronger electrostatic connections within the interlayer space, which strengthens the connection between the layers. Moreover, the electrons of V and O are farther apart in PyVO and the V−O electron overlapping is also decreased, indicating the lower V−O covalency in PyVO compared to VOH. The changes in V−O bonds imply the distortion of $[VO_6]$ octahedra in PyVO. To precisely illustrate this distortion, k^3-weighted Fourier transform (Figure 2c), *q*-space oscillations of different coordination atoms (Figure S5), and corresponding wavelet transform (Figure 2d and Figure S6) are derived from the extended X-ray absorption fine structure (EXAFS). As presented in Figure 2c, the peaks at approximately 1.9 Å are assigned to V−O interatomic distances of the first coordination sphere.[23,43] Notably, in PyVO, the V−O peak shifts to a higher radial distance by around 0.06 Å compared to VOH. This shift indicates the elongation of the V−O bonds, confirming the presence of polyhedra distortion. In the case of octahedral coordination, V^{4+} has a larger ionic radius of 72 pm compared to that of 68 pm for V^{5+}.[20] As verified by the XPS spectra of V $2p_{3/2}$, the ratio of V^{4+} in PyVO is 16.2%, higher than the 9.0% in VOH, leading to the longer V−O bonds in PyVO. The EXAFS fit is performed on PyVO and VOH to further investigate the variations in the coordination environment. The fitting curves and results are shown in Figure S7 and Table 1.

Table 1. Interatomic Distances of Both Samples from EXAFS Fitting[a]

Sample	Atom pair	Distance	*N*	σ^2 (10^{-3} Å^2)
PyVO	V−O1	(1.77 ± 0.01) Å	2	6.6 ± 1.8
	V−O2	(2.00 ± 0.01) Å	2	6.6 ± 1.8
	V−O3	(2.37 ± 0.01) Å	2	6.6 ± 1.8
	V−V1	(3.03 ± 0.02) Å	2	14.6 ± 3.3
	V−V2	(3.37 ± 0.02) Å	2.5	14.6 ± 3.3
	V−V3	(3.56 ± 0.03) Å	2.5	14.6 ± 3.3
VOH	V−O1	(1.72 ± 0.01) Å	2	8.6 ± 1.9
	V−O2	(1.93 ± 0.01) Å	3	8.6 ± 1.9
	V−O3	(2.30 ± 0.01) Å	1	8.6 ± 1.9
	V−V1	(3.04 ± 0.01) Å	2	10.2 ± 1.5
	V−V2	(3.38 ± 0.01) Å	2.5	10.2 ± 1.5
	V−V3	(3.59 ± 0.01) Å	2.5	10.2 ± 1.5

[a]*N* is coordination number, and σ^2 is Debye−Waller factor.

Three incremental V−O distances (V−O1, V−O2, and V−O3) are adopted to simulate the bond lengths in the $[VO_6]$ octahedron. As illustrated in Figure 2e, in a single $[VO_6]$ octahedron, the V−O1 distance represents the shortest one among the four V−O bonds within the *ab* plane, and the shorter of the two V−O bonds along the *c* axis. V−O2 stands for the other three V−O bonds within the *ab* plane. V−O3 is the longer V−O bond along the *c* axis. In PyVO, the fitted V−O distances (V−O1, V−O2, and V−O3) are all longer than those in VOH, agreeing with the k^3-weighted Fourier transform results in Figure 2b. The coordination numbers of V−O1, V−O2, and V−O3 in PyVO and VOH are 2, 2, 2 and 2, 3, 1, respectively, indicating the longest V−O distance (V−O3) accounts for a larger proportion in PyVO. A part of V−O

https://doi.org/10.1021/acsenergylett.4c02709
ACS Energy Lett. 2024, 9, 5492−5501

bonds in the *ab* plane with V−O2 distance are elongated to the V−O3 distance, resulting in the increase in the coordination number of V−O3 and the decrease in the coordination number of V−O2. The average V−O bond length can be described by

$$\bar{R} = \frac{R(\mathrm{V{-}O1}) \times N1}{6} + \frac{R(\mathrm{V{-}O2}) \times N2}{6} + \frac{R(\mathrm{V{-}O3}) \times N3}{6} \quad (1)$$

where $R(\mathrm{V{-}O1})$, $R(\mathrm{V{-}O2})$, and $R(\mathrm{V{-}O3})$ are the interatomic distance values of V−O1, V−O2, and V−O3. *N*1, *N*2, and *N*3 are the corresponding coordination numbers. PyVO has an average V−O bond length of 2.05 Å, larger than that of VOH (1.92 Å), validating the elongation of V−O bonds and the distortion of [VO_6] octahedra in PyVO compared with those in VOH. Additionally, the *R*-space signal in Figure 2b and its fitting results reveal that the V−V interatomic distance and the V−V coordination number remain almost invariant, suggesting the identical V 3*d*−V 3*d* direct interaction in both samples. The invariant V−V distance and the longer V−O distance in PyVO indicate the variation in V−O−V bond angles, in comparison with those in VOH. Based on the ligand field theory (LFT), the above-discussed changes in local coordination environment can modulate the electron structures, via altering the interactions between the electron orbitals of vanadium and oxygen.[44]

The V *L*-edge and the O *K*-edge XANES spectra of PyVO and VOH are shown in Figure 3a. The V L_3 and L_2 peaks originate from the electron transitions from V $2p_{3/2}$ and $2p_{1/2}$ to the unoccupied V 3*d* states, respectively.[45] PyVO exhibits lower intensities of V L_3 and L_2 peaks, compared with those in VOH, indicating the higher occupancy of V 3*d* orbitals and the lower valence of vanadium in PyVO.[46] The multiplets observed in V L_3 peak are associated with the symmetry and spin state of the ground state.[47] The O *K*-edge spectra is attributed to electron transitions from the O 1*s* to unoccupied O*p* character orbitals, which correspond to the t_{2g}* (V 3*d*−O 2*p*, π antibonding combination), e_g* (V 3*d*−O 2*p*, σ antibonding combination), and V 4*sp*−O 2*p* antibonding orbitals, respectively.[45] The antibonding orbitals have a higher energy level in comparison with the bonding orbitals. V 3*d* electrons has higher energy level than O 2*p* electrons, tending to occupy the antibonding orbitals.[48,49] Specifically, the electron structures of V^{5+} and V^{4+} are [Ar]$3d^0$ and [Ar]$3d^1$, respectively. The single 3*d* electron of V^{4+} ($3d^1$) tends to occupy a portion of the t_{2g}* state, which determines the electrochemical potential of the cathode. The e_g* and V 4*sp*−O 2*p* antibonding orbitals in both samples are empty and not engaged in the electrochemical reaction. The decrease in the intensity of t_{2g}* peak indicates its higher occupancy in PyVO.[23] The decreased intensities of e_g* and V 4*sp*−O 2*p* peaks in PyVO are attributed to the lower V−O covalency.[45] Figure 3b is the Gaussian fitting results of t_{2g}* and e_g* peaks for PyVO and VOH. The [VO_6] octahedra in both samples present C_{4v} symmetry, leading to the further split of t_{2g}* and e_g* orbitals into *e** ($3d_{yz}$, $3d_{xz}$), b_2* ($3d_{xy}$), a_1* (d_{z^2}), and b_1* ($d_{x^2-y^2}$) states in increasing energy.[21,50] The single 3*d* electron of V^{4+} ($3d^1$) occupies *e** ($3d_{yz}$, $3d_{xz}$) state, which is the lowest unoccupied state in V^{5+} situation.[23] Therefore, the *e** ($3d_{yz}$, $3d_{xz}$) state of PyVO is higher filled and the ratio of *e** ($3d_{yz}$, $3d_{xz}$) peak decreases because of its higher occupancy in PyVO. Moreover, the *e** ($3d_{yz}$, $3d_{xz}$) peak shifts to lower energy in PyVO, compared with that of VOH, indicating the lower energy level of the lowest unoccupied state in PyVO, which contributes to the increase in electrochemical potential. The peaks of b_2* and e_g* also shift to lower energies, indicating the decrease in the overall energy of the antibonding orbital. Due to the elongated V−O bonds in PyVO, the V−O covalent interactions are weakened.[51] The lower V−O covalency in PyVO reduces the energy gap between the bonding and antibonding orbitals, leading to the decrease in the energy level of the antibonding orbitals (*e**, b_2* and e_g*).[48,52] The valence band region of XPS spectra, as shown in Figure 3c, reveals that the predominant band in PyVO, corresponding to the O 2*p* contributions,[53] shifts toward higher binding energy compared to that in VOH. Figure S8 shows the ultraviolet photoelectron spectroscopy (UPS) of both samples. The signal of the O 2*p* band ranges from 3 to 10 eV.[54] The predominant peak at ∼15.5 eV is attributed to the secondary electrons.[55] Compared with VOH, the O 2*p* peak of PyVO shifts toward higher binding energy by about 0.3 eV, as illustrated in the inset, providing corroborative evidence for the lower energy level of the O 2*p* band in PyVO. This shift is speculated to be due to the electron withdrawing exerted by Pyr^+ cations on the lattice oxygen.[18,56] The low-intensity band around 2 eV in Figure 3c is contributed by V 3*d*, dominated by the *e** ($3d_{yz}$, $3d_{xz}$) state.[53] In PyVO, the band of V 3*d* shifts to higher binding energy by about 0.4 eV compared to VOH and the band is also broader than that in VOH. As illustrated in Figure 3d, the shift of V 3*d* band toward higher binding energy indicates a decrease in the energy level of the *e** ($3d_{yz}$, $3d_{xz}$) state in PyVO, which constitutes the V 3*d* band. The decreased energy level of the *e** ($3d_{yz}$, $3d_{xz}$) state is also validated by the fitting results of the O *K*-edge XANES. Furthermore, the broadening of the V 3*d* band in PyVO can be

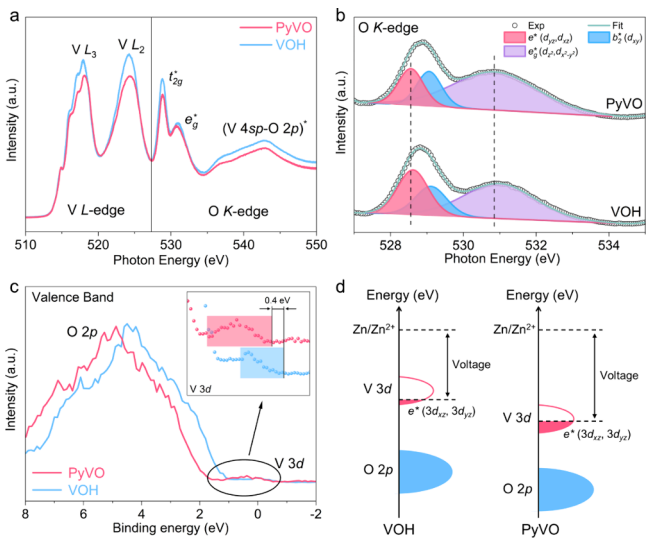

Figure 3. Band energy information on PyVO and VOH. (a) V *L*-edge and O *K*-edge XANES spectra of both samples. The lower amplitude of PyVO indicates its higher 3*d* orbital occupancy and lower valence state of vanadium. (b) Gaussian fitting of t_{2g}* and e_g* peaks for both samples. Due to the C_{4v} symmetry of [VO_6] octahedra in both samples, the t_{2g}* antibonding orbital splits into *e and b_2* orbitals. (c) The valence-band region of XPS spectra for PyVO and VOH. Bands of O 2*p* and V 3*d* shift to higher binding energy in PyVO, further demonstrating the lower energy level of V 3*d* and O 2*p* bands. (d) Schematic illustration of energy diagram of both samples. PyVO has the lower energy state of the V 3*d* band, which is dominated by the *e** ($3d_{yz}$, $3d_{xz}$) state.**

https://doi.org/10.1021/acsenergylett.4c02709
ACS Energy Lett. 2024, 9, 5492−5501

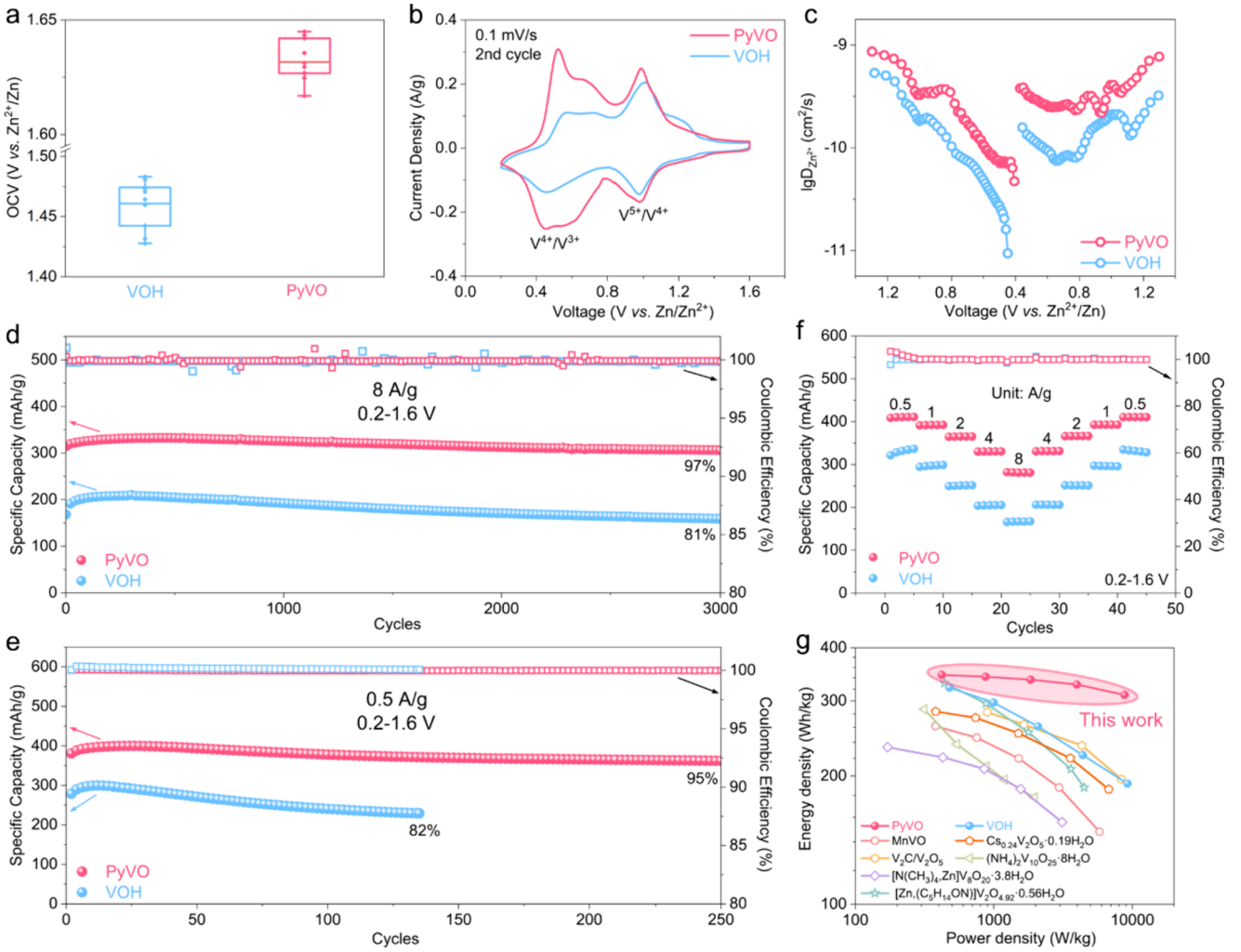

Figure 4. Electrochemical properties of PyVO and VOH. (a) Open-circuit voltage statistics from ten batteries. Intercalated Pyr^+ ions influence the splitting of the ligand field and result in a higher open-circuit voltage. (b) CV curves of PyVO and VOH collected at a sweep rate of 0.1 mV/s. PyVO presents an enhanced capacity contribution from the V^{4+}/V^{3+} redox pair around 0.5 V. (c) Zn^{2+} diffusion coefficients from GITT tests; PyVO has faster ion diffusion in the charging/discharging process. Cycling performance at (d) 8 A/g and (e) 0.5 A/g. (f) Rate performance at current densities from 0.5 A/g to 8 A/g, supported by the faster mass transfer. (g) Ragone plots of PyVO, VOH, and reported cathode materials.

attributed to its higher ratio of V^{4+}, which causes an increased electron occupancy in the e^* ($3d_{yz}$, $3d_{xz}$) state. The lower-energy level of the V 3*d* band, which is dominated by the e^* ($3d_{yz}$, $3d_{xz}$) state, increases the energy gap with the Fermi level of Zn metal, resulting in an increased electrochemical potential of PyVO compared to VOH.[23,52]

Figure 4a presents a comparison of the open-circuit voltages (OCV) of both samples. The average OCV of PyVO is 1.63 V, higher than that of VOH (1.46 V), which is attributed to the lower energy of the e^* ($3d_{yz}$, $3d_{xz}$) state enlarging the energy gap with Zn, as illustrated in Figure 3d. Due to the distorted local structure, the electrochemical potential of PyVO is significantly enhanced. Figure S9 shows the CV curves of PyVO in the initial three cycles at a scan rate of 0.1 mV/s. Two pairs of peaks are observed in the curves. The peaks around 1.0 and 0.5 V relate to the redox pairs of V^{5+}/V^{4+} and V^{4+}/V^{3+}, respectively.[20,57] As corroborated by the ex situ XPS spectra of Zn 2*p* and V $2p_{3/2}$ in the initial cycle (Figure S10), when the PyVO cathode is discharged, V^{5+} are reduced to V^{4+} and V^{4+} are subsequently reduced to V^{3+} with the insertion of Zn^{2+}. During charging, V^{4+} and V^{3+} are oxidated oppositely as the extraction of Zn^{2+}. Compared to that of VOH (Figure S9a), the highly overlapped CV curves of PyVO in the first three cycles indicate high reversibility. Figure 4b presents the CV curves of PyVO and VOH, measured at a scan rate of 0.1 mV/s during the second cycle. For PyVO, the current density of the V^{4+}/V^{3+} redox pair is much higher than that of VOH, indicating a more complete reaction of the V^{4+}/V^{3+} pair in PyVO. Furthermore, the voltage gaps of redox pairs in PyVO (9 mV for V^{5+}/V^{4+} and 68 mV for V^{4+}/V^{3+}) are narrower than those in VOH (33 mV for V^{5+}/V^{4+} and 120 mV for V^{4+}/V^{3+}), suggesting lower polarization in PyVO. Figure S11 shows the CV contours of PyVO and VOH, scanned at various scan rates from 0.2 to 1.2 mV/s. As the scan rate increases, the reduction peaks shift to higher voltages and the oxidation peaks toward lower voltages because of the electrochemical polarization during the zincation and dezincation. EIS spectra for both samples, captured at the OCV states before and after three cycles of the CV test (0.1 mV/s), are shown in Figure S12. The semicircle and the oblique tail in EIS spectra were associated with the charge transfer resistance (R_{ct}) and Warburg resistance (W_0), respectively.[58] After the CV test, the

https://doi.org/10.1021/acsenergylett.4c02709
ACS Energy Lett. 2024, 9, 5492−5501

electrodes are activated, significantly decreasing the R_{ct} values of both samples. PyVO exhibits a lower R_{ct} than VOH, indicating improved charge transfer in PyVO. The smaller R_{ct} of PyVO is due to its larger interlayer spacing facilitating the interfacial ion intercalation/deintercalation and the higher ratio of V^{4+} improving the electronic conductivity.[20] The Warburg's slope becomes steeper after CV test, indicating the improved ion diffusion after the activation of the CV test.[59] The in situ EIS spectra for the activated PyVO cathode during the discharging and charging process are shown in Figure S13. During discharging, the R_{ct} becomes larger and the Warburg's slope becomes smaller, indicating the more sluggish ion and electron transfer rate. With the insertion of Zn^{2+}, the spatial site resistance increases, which suppresses the subsequent Zn^{2+} intercalation and diffusion, resulting in the increasing interfacial charge transfer resistance and bulk ion diffusion resistance during discharging.[60] The ex situ XRD patterns of PyVO in the initial cycle are shown in Figure S14. The (001) plane shifts from 2θ = 6.4° to 7.6° during discharging, indicating the narrowing interlayer spacing by 14.5%, from 13.8 to 11.8 Å, due to the increased electrostatic attraction between inserted Zn^{2+} and negatively charged [VO] slabs.[29] The contracted interlayer spacing also leads to increases in R_{ct} and W_0 during discharging. With the extraction of Zn^{2+} during charging, the R_{ct} and W_0 gradually recover to the initial level and the (001) peak moves back to the pristine position, suggesting excellent electrochemical and structural reversibility of PyVO. The ex situ XRD patterns of VOH in the initial cycle are shown in Figure S15. To figure out the role of Pyr^+ cations in the lattice, Figure S16 shows the interlayer spacings of the (001) plane for both samples during charging/discharging extracted from the ex situ XRD patterns. As the VOH cathode is discharged from the pristine state to 1.1 V, the inserted Zn^{2+} ions expand the interlayer spacing of the (001) plane from 12.1 to 13.4 Å. When discharged further, the interlayer spacing of VOH maximizes and begins to shrink due to the electrostatic attraction between the [VO] slabs and Zn^{2+}, as discussed above. Upon the discharging process from 1.1 to 0.7 V, corresponding to the V^{5+}/V^{4+} redox pair, the interlayer spacing of VOH decreases from 13.4 to 12.3 Å, by 8.2%, larger than that of PyVO (5.8%, from 13.7 to 12.9 Å). The specific capacities delivered from 1.1 to 0.7 V for VOH and PyVO are 153 and 146 mAh/g, respectively, indicating almost identical amounts of inserted Zn^{2+} ions in both samples for this voltage range. The smaller shrinkage of the (001) plane in PyVO indicates the preintercalated Pyr^+ cations can effectively buffer the layer spacing expansion and alleviate the volume strain during cycling.[26,28] This buffering effect is possibly due to the lattice strengthened by the electrostatic interaction between Pyr^+ cations and the [VO] slab, as illustrated by ELF in Figure 2b. When discharged from 0.7 to 0.2 V, which is the voltage range of the V^{4+}/V^{3+} redox pair, VOH delivers a capacity of 142 mAh/g in this voltage range with (001) plane shrinkage of 2.4% (12.3 to 12.0 Å). The corresponding values of PyVO are 250 mAh/g and 7.8% (12.9 to 11.9 Å), respectively. This indicates the lattice of VOH tends to be saturated after being discharged to 0.7 V, resulting in the limited interlayer spacing for Zn^{2+} to insert and diffuse during the discharging process from 0.7 to 0.2 V. While for PyVO, due to the buffering effect of Pyr^+ cations, the lattice spacing is wider than that of VOH, leading to the more complete reaction of the V^{4+}/V^{3+} pair as shown in the CV curves (Figure 4a), which contributes to the higher specific capacity of PyVO. The Zn^{2+} diffusion coefficients ($D_{Zn^{2+}}$) are measured by the galvanostatic intermittent titration technique (GITT). As shown in Figure 4c, PyVO exhibits a higher $D_{Zn^{2+}}$ ($10^{-9.7}$–$10^{-9.1}$ cm^{-2}/s) than that of VOH ($10^{-10.1}$–$10^{-9.5}$ cm^{-2}/s) during the charging process. Similarly, during the discharging process, the $D_{Zn^{2+}}$ values for PyVO range from $10^{-10.3}$ to $10^{-9.1}$ cm^{-2}/s, exceeding those of VOH, which range from $10^{-11.0}$ to $10^{-9.3}$ cm^{-2}/s. This improved performance is attributed to the expanded layer spacing in PyVO for ion diffusion. Additionally, the replacement of lattice water with organic cations reduces the interactions between intercalated Zn^{2+} and lattice oxygen, further enhancing diffusion efficiency.[61] $D_{Zn^{2+}}$ decreases with the reducing voltage during discharging, while in the charging, $D_{Zn^{2+}}$ become higher with the increasing voltage. This can be attributed to the variation of interactions among the inserted zinc ions during intercalation and deintercalation of Zn^{2+}.

As shown in Figure S17, the voltage profiles of PyVO at 0.5 A/g with a voltage range of 0.2–1.6 V are highly overlapped with a specific capacity of 412 mAh/g in the first three cycles, corroborating the CV tests. The voltage profiles reveal two distinct charge and discharge plateaus. The first plateau, ranging from 1.1 to 0.7 V, corresponds to the redox pair of V^{5+}/V^{4+}. The second plateau, observed from 0.6 to 0.3 V, is associated with the redox pair of V^{4+}/V^{3+}. The voltage ranges of these plateaus are consistent with the peak positions in the CV curves (Figure 4b). Figure S18 shows the voltage profiles at the 50th cycle under a current density of 4 A/g. Owing to the enhanced electrochemical kinetics, the curve of the V^{5+}/V^{4+} redox pair in PyVO appears at a higher voltage compared with VOH. PyVO delivers a specific capacity of 339 mAh/g at 4 A/g, while VOH delivers a lower capacity of 227 mAh/g. The more thorough the reaction of V^{4+} during electrochemical process, the faster the Zn^{2+} diffusion and the smaller the charge transfer resistance, leading to less electrochemical polarization and the higher capacity of PyVO. During the long-term cycling test at 8 A/g with the voltage range of 0.2–1.6 V (Figure 4d), PyVO delivers an initial specific capacity of 314 mAh/g, showing a significant improvement compared with the capacity of 168 mAh/g for VOH. After 3000 cycles, the capacity retention of PyVO is 97%, higher than 81% of VOH. The cycle performance at 4 A/g (0.2–1.6 V) is shown in Figure S19. PyVO maintains 98% of its initial capacity after 1000 cycles, which is higher than that of VOH, which is 90%. As shown in Figure 4e, PyVO exhibits excellent cycle stability at 0.5 A/g with a voltage range of 0.2–1.6 V, maintaining 95% of its initial capacity after 250 cycles with a specific capacity of 400 mAh/g. In contrast, VOH shows a rapid capacity fading, maintaining only 82% of its initial capacity after 135 cycles. As previously discussed, the electrostatic interaction between Pyr^+ and [VO] framework stabilizes the lattice and buffers the volume strain during the charging and discharging process.[26] Therefore, the degradation of the layer structure is alleviated, which contributes to the stable cycling performance. Cycling tests with a wider voltage range (0.2–1.8 V) are also conducted. In Figure S20, as the voltage range increases, VOH suffers significant capacity fading by 54% after 3000 cycles at 8 A/g, much more severe than the fading at the range of 0.2–1.6 V. For PyVO, the capacity retention of 93% can be achieved at 8 A/g, respectively, showing excellent stability in the wider voltage range. As mentioned above, the altered electronic structure leads to the higher average open-circuit voltage of PyVO (1.63 V) compared with that of VOH (1.46 V). The lifted OCV endows the PyVO cathode with higher

https://doi.org/10.1021/acsenergylett.4c02709
ACS Energy Lett. 2024, 9, 5492–5501

thermodynamic stability at a relatively wide voltage range, also contributing to its enhanced cycling stability. In contrast, VOH experiences much more severe capacity fading when the upper cutoff voltage is raised to 1.8 V. The rate performances of both samples are shown in Figure 4f. PyVO delivers a specific capacity of 412 mAh/g at a current density of 0.5 A/g, higher than that in VO_2, $Na_2V_6O_{16}\cdot 1.63H_2O$, and $Mn_xV_2O_5\cdot nH_2O$.[20,62,63] In contrast, VOH has an initial specific capacity of 322 mAh/g at the same current density, increased to 336 mAh/g after 4 cycles, while PyVO retains its initial value. As the current density increases to 1, 2, 4, and 8 A/g, PyVO delivers specific capacities of 392, 365, 331, and 282 mAh/g, respectively, which are higher than those of VOH (299, 253, 207, and 168 mAh/g, respectively). The capacity retention of PyVO at 8 A/g is 68.5%, which outperforms VOH's retention of 52.2%. The higher specific capacity and the better rate performance of the PyVO cathode can be attributed to its expanded interlayer spacing facilitating ion diffusion and the smaller R_{ct} accelerating the charge transfer process. When the current density returns to 0.5 A/g, the specific capacity of PyVO recovers to its initial value, indicating a great structural stability and excellent electrochemical reversibility.[20] Figure 4g shows the Ragone plots of PyVO and VOH. PyVO exhibits an energy density of 346 Wh/kg at 421 W/kg and 310 Wh/kg at 8789 W/kg at material level, outperforming VOH (323 Wh/kg at 479 W/kg and 192 Wh/kg at 9217 W/kg), as well as many previously reported cathodes.[20,29,30,32,64,65] The enhanced electrochemical kinetics of PyVO lead to its outstanding energy density. Overall, the substitution of H_2O molecules with Pyr^+ cations induces stronger electrostatic interactions between Pyr^+ cations and the [VO] framework. This modification enhances the electrochemical potential of the PyVO cathode via distorting the [VO_6] octahedra and altering the ligand field. The introduced Pyr^+ cations also play a crucial role in strengthening the structural stability and improving the electrochemical kinetics during the Zn^{2+} insertion and extraction processes.

The local and electronic structures of hydrate vanadium oxide are modulated through replacing electroneutral water molecules by organic 1-butyl-1-methylpyrrolidinium cations. The elongation of V−O bonds and distortion on [VO_6] octahedra alter the ligand field surrounding vanadium cations and decrease the energy level of e^* ($3d_{yz}$, $3d_{xz}$) state to raise the electrochemical potential. The attained cathode obtains a high open-circuit voltage of 1.63 V in comparison with that of the pristine hydrate vanadium oxide (1.46 V). The flexible organic cations also facilitate Zn^{2+} diffusion by buffering the lattice expansion/shrinkage and enhance the stability of layer structure via the exerted stronger electrostatic interaction between [VO] layers. As a result, PyVO delivers a superior specific capacity of 412 mAh/g, with a capacity retention of 95% after 250 cycles at 0.5 A/g. This work not only discloses the impacts of local structure on the energy level of reactive electron orbitals but also provides insight into designing advanced electrode materials for next-generation high-performance rechargeable batteries.

■ ASSOCIATED CONTENT

Data Availability Statement

Data will be made available on request.

Supporting Information

The Supporting Information is available free of charge at https://pubs.acs.org/doi/10.1021/acsenergylett.4c02709.

Additional experimental methods, calculations, data and figures, including synthesis, electrode preparations, electrochemical testing, DFT calculations, TEM images of PyVO, XPS spectra of N 1s, *q*-space oscillations and 3D wavelet transform of XANES spectra, EXAFS fittings, UPS spectra, CV curves and contours, EIS spectra, ex situ XPS/XRD spectra, voltage profiles, and cycling performance at 4 A/g and 8 A/g with 0.2−1.8 V (PDF)

■ AUTHOR INFORMATION

Corresponding Authors

Guozhong Cao − *Department of Materials Science and Engineering, University of Washington, Seattle, Washington 98195, United States*; Email: gzcao@uw.edu

Chaofeng Liu − *Interdisciplinary Materials Research Center, School of Materials Science and Engineering, Tongji University, Shanghai 201804, China*; orcid.org/0000-0003-2942-1418; Email: chaofeng@tongji.edu.cn

Authors

Heng Liu − *Interdisciplinary Materials Research Center, School of Materials Science and Engineering, Tongji University, Shanghai 201804, China*

Huanhuan Niu − *Interdisciplinary Materials Research Center, School of Materials Science and Engineering, Tongji University, Shanghai 201804, China*

Wei-Hsiang Huang − *National Synchrotron Radiation Research Center (NSRRC), Hsinchu 300092, Taiwan*; orcid.org/0000-0001-9503-0373

Ting Shen − *Department of Materials Science and Engineering, Clemson University, Clemson, South Carolina 29634, United States*

Changyuan Li − *Interdisciplinary Materials Research Center, School of Materials Science and Engineering, Tongji University, Shanghai 201804, China*

Chun-Chi Chang − *Graduate Institute of Applied Science and Technology, National Taiwan University of Science and Technology, Taipei 10607, Taiwan*

Menghao Yang − *Interdisciplinary Materials Research Center, School of Materials Science and Engineering, Tongji University, Shanghai 201804, China*; orcid.org/0000-0001-7926-5113

Chenlong Gao − *Interdisciplinary Materials Research Center, School of Materials Science and Engineering, Tongji University, Shanghai 201804, China*

Long Yang − *Interdisciplinary Materials Research Center, School of Materials Science and Engineering, Tongji University, Shanghai 201804, China*

Quan Zong − *College of Materials and Chemistry, China Jiliang University, Hangzhou, Zhejiang 310018, China*

Yanzhong Pei − *Interdisciplinary Materials Research Center, School of Materials Science and Engineering, Tongji University, Shanghai 201804, China*; orcid.org/0000-0003-1612-3294

Complete contact information is available at: https://pubs.acs.org/10.1021/acsenergylett.4c02709

Notes

The authors declare no competing financial interest.

https://doi.org/10.1021/acsenergylett.4c02709
ACS Energy Lett. 2024, 9, 5492−5501

■ ACKNOWLEDGMENTS

This work is financially supported by the National Natural Science Foundation of China (52102277 and 52302322) and the Fundamental Research Funds for the Central Universities, conducted by Tongji University. Dr. Liu appreciates the XAFS support by Dr. Jingpeng Zhao from Quantum Design China. The authors acknowledge the Experimental Center of Materials Science and Engineering in Tongji University. Research facilities of soft-XAS was provided by the beamline of TLS BL20A1, National Synchrotron Radiation Research Center (NSRRC) in Taiwan.

■ REFERENCES

(1) Xie, J.; Lu, Y. A Retrospective on Lithium-Ion Batteries. *Nat. Commun.* **2020**, *11*, 2499.
(2) Chao, D.; Zhou, W.; Xie, F.; Ye, C.; Li, H.; Jaroniec, M.; Qiao, S. Z. Roadmap for Advanced Aqueous Batteries: From Design of Materials to Applications. *Sci. adv.* **2020**, *6*, No. eaba4098.
(3) Jia, X.; Liu, C.; Neale, Z. G.; Yang, J.; Cao, G. Active Materials for Aqueous Zinc Ion Batteries: Synthesis, Crystal Structure, Morphology, and Electrochemistry. *Chem. Rev.* **2020**, *120*, 7795−7866.
(4) Yadav, G. G.; Gallaway, J. W.; Turney, D. E.; Nyce, M.; Huang, J.; Wei, X.; Banerjee, S. Regenerable Cu-Intercalated MnO_2 Layered Cathode for Highly Cyclable Energy Dense Batteries. *Nat. Commun.* **2017**, *8*, 14424.
(5) Cui, S.; Zhang, D.; Gan, Y. Traditional Electrochemical Zn^{2+} Intercalation/Extraction Mechanism Revisited: Unveiling Ion-Exchange Mediated Irreversible Zn^{2+} Intercalation for the δ-MnO_2 Cathode in Aqueous Zn Ion Batteries. *Adv. Energy Mater.* **2024**, *14*, No. 2302655.
(6) Trócoli, R.; Mantia, F. L. An Aqueous Zinc-Ion Battery Based on Copper Hexacyanoferrate. *ChemSusChem* **2015**, *8*, 481−485.
(7) Liu, J.; Shen, Z.; Lu, C. Z. Research Progress of Prussian Blue and Its Analogues for Cathodes of Aqueous Zinc Ion Batteries. *J. Mater. Chem. A* **2024**, *12*, 2647−2672.
(8) Yi, H.; Qin, R.; Ding, S.; Wang, Y.; Li, S.; Zhao, Q.; Pan, F. Structure and Properties of Prussian Blue Analogues in Energy Storage and Conversion Applications. *Adv. Funct. Mater.* **2021**, *31*, No. 2006970.
(9) Cui, H.; Wang, T.; Huang, Z.; Liang, G.; Chen, Z.; Chen, A.; Wang, D.; Yang, Q.; Hong, H.; Fan, J.; Zhi, C. High-Voltage Organic Cathodes for Zinc-Ion Batteries through Electron Cloud and Solvation Structure Regulation. *Angew. Chem., Int. Ed.* **2022**, *61*, No. e202203453.
(10) Cui, H.; Ma, L.; Huang, Z.; Chen, Z.; Zhi, C. Organic Materials-Based Cathode for Zinc Ion Battery. *SmartMat* **2022**, *3*, 565−581.
(11) Soundharrajan, V.; Sambandam, B.; Kim, S.; Alfaruqi, M. H.; Putro, D. Y.; Jo, J.; Kim, S.; Mathew, V.; Sun, Y. K.; Kim, J. $Na_2V_6O_{16}$·$3H_2O$ Barnesite Nanorod: An Open Door to Display a Stable and High Energy for Aqueous Rechargeable Zn-Ion Batteries as Cathodes. *Nano Lett.* **2018**, *18*, 2402−2410.
(12) Guo, Q.; Li, W.; Li, X.; Zhang, J.; Sabaghi, D.; Zhang, J.; Zhang, B.; Li, D.; Du, J.; Chu, X.; Chung, S.; Cho, K.; Nguyen, N. N.; Liao, Z.; Zhang, Z.; Zhang, X.; Schneider, G. F.; Heine, T.; Yu, M.; Feng, X. Proton-Selective Coating Enables Fast-Kinetics High-Mass-Loading Cathodes for Sustainable Zinc Batteries. *Nat. Commun.* **2024**, *15*, 2139.
(13) Song, M.; Tan, H.; Chao, D.; Fan, H. J. Recent Advances in Zn-Ion Batteries. *Adv. Funct. Mater.* **2018**, *28*, No. 1802564.
(14) Mathew, V.; Sambandam, B.; Kim, S.; Kim, S.; Park, S.; Lee, S.; Alfaruqi, M. H.; Soundharrajan, V.; Islam, S.; Putro, D. Y.; Hwang, J. Y.; Sun, Y. K.; Kim, J. Manganese and Vanadium Oxide Cathodes for Aqueous Rechargeable Zinc-Ion Batteries: A Focused View on Performance, Mechanism, and Developments. *ACS Energy Lett.* **2020**, *5*, 2376−2400.
(15) Sun, Q.; Cheng, H.; Yuan, Y.; Liu, Y.; Nie, W.; Zhao, K.; Wang, K.; Yao, W.; Lu, X.; Lu, J. Uncovering the Fundamental Role of Interlayer Water in Charge Storage for Bilayered $V_2O_5 \cdot nH_2O$ Xerogel Cathode Materials. *Adv. Energy Mater.* **2023**, *13*, No. 2202515.
(16) Liu, Y.; Xu, J.; Li, J.; Yang, Z.; Huang, C.; Yu, H.; Zhang, L.; Shu, J. Pre-Intercalation Chemistry of Electrode Materials in Aqueous Energy Storage Systems. *Coord. Chem. Rev.* **2022**, *460*, 214477.
(17) Yan, M.; He, P.; Chen, Y.; Wang, S.; Wei, Q.; Zhao, K.; Xu, X.; An, Q.; Shuang, Y.; Shao, Y.; Mueller, K. T.; Mai, L.; Liu, J.; Yang, J. Water-Lubricated Intercalation in V_2O_5·nH_2O for High-Capacity and High-Rate Aqueous Rechargeable Zinc Batteries. *Adv. Mater.* **2018**, *30*, No. 1703725.
(18) Jia, X.; Liu, C.; Wang, Z.; Huang, D.; Cao, G. Weakly Polarized Organic Cation-Modified Hydrated Vanadium Oxides for High-Energy Efficiency Aqueous Zinc-Ion Batteries. *Nano-Micro Lett.* **2024**, *16*, 129.
(19) Liu, S.; Zhu, H.; Zhang, B.; Li, G.; Zhu, H.; Ren, Y.; Geng, H.; Yang, Y.; Liu, Q.; Li, C. C. Tuning the Kinetics of Zinc-Ion Insertion/Extraction in V_2O_5 by in Situ Polyaniline Intercalation Enables Improved Aqueous Zinc-Ion Storage Performance. *Adv. Mater.* **2020**, *32*, No. 2001113.
(20) Liu, C.; Neale, Z.; Zheng, J.; Jia, X.; Huang, J.; Yan, M.; Tian, M.; Wang, M.; Yang, J.; Cao, G. Expanded Hydrated Vanadate for High-Performance Aqueous Zinc-Ion Batteries. *Energy Environ. Sci.* **2019**, *12*, 2273−2285.
(21) Li, J.; McColl, K.; Lu, X.; Sathasivam, S.; Dong, H.; Kang, L.; Li, Z.; Zhao, S.; Kafizas, A. G.; Wang, R.; Brett, D. J. L.; Shearing, P. R.; Corà, F.; He, G.; Carmalt, C. J.; Parkin, I. P. Multi-Scale Investigations of δ-$Ni_{0.25}V_2O_5$·nH_2O Cathode Materials in Aqueous Zinc-Ion Batteries. *Adv. Energy Mater.* **2020**, *10*, No. 2000058.
(22) Zheng, J.; Liu, C.; Tian, M.; Jia, X.; Jahrman, E. P.; Seidler, G. T.; Zhang, S.; Liu, Y.; Zhang, Y.; Meng, C.; Cao, G. Fast and Reversible Zinc Ion Intercalation in Al-Ion Modified Hydrated Vanadate. *Nano Energy* **2020**, *70*, No. 104519.
(23) Wang, Y.; Wei, S.; Qi, Z.-H.; Chen, S.; Zhu, K.; Ding, H.; Cao, Y.; Zhou, Q.; Wang, C.; Zhang, P.; Guo, X.; Yang, X.; Wu, X.; Song, L. Intercalant-Induced V t_{2g} Orbital Occupation in Vanadium Oxide Cathode toward Fast-Charging Aqueous Zinc-Ion Batteries. *Proc. Natl. Acad. Sci. U. S. A.* **2023**, *120*, No. e2217208120.
(24) Yang, Y.; Tang, Y.; Fang, G.; Shan, L.; Guo, J.; Zhang, W.; Wang, C.; Wang, L.; Zhou, J.; Liang, S. Li^+ Intercalated V_2O_5·nH_2O with Enlarged Layer Spacing and Fast Ion Diffusion as an Aqueous Zinc-Ion Battery Cathode. *Energy Environ. Sci.* **2018**, *11*, 3157−3162.
(25) Zhao, Q.; Song, A.; Ding, S.; Qin, R.; Cui, Y.; Li, S.; Pan, F. Preintercalation Strategy in Manganese Oxides for Electrochemical Energy Storage: Review and Prospects. *Adv. Mater.* **2020**, *32*, No. 2002450.
(26) Chen, S.; Li, K.; Hui, K. S.; Zhang, J. Regulation of Lamellar Structure of Vanadium Oxide Via Polyaniline Intercalation for High-Performance Aqueous Zinc-Ion Battery. *Adv. Funct. Mater.* **2020**, *30*, No. 2003890.
(27) Ma, X.; Cao, X.; Yao, M.; Shan, L.; Shi, X.; Fang, G.; Pan, A.; Lu, B.; Zhou, J.; Liang, S. Organic-Inorganic Hybrid Cathode with Dual Energy-Storage Mechanism for Ultrahigh-Rate and Ultralong-Life Aqueous Zinc-Ion Batteries. *Adv. Mater.* **2022**, *34*, No. 2105452.
(28) Yao, Z.; Zhang, W.; Ren, X.; Yin, Y.; Zhao, Y.; Ren, Z.; Sun, Y.; Lei, Q.; Wang, J.; Wang, L.; Ji, T.; Huai, P.; Wen, W.; Li, X.; Zhu, D.; Tai, R. A Volume Self-Regulation MoS_2 Superstructure Cathode for Stable and High Mass-Loaded Zn-Ion Storage. *ACS Nano* **2022**, *16*, 12095−12106.
(29) Zong, Q.; Zhuang, Y.; Liu, C.; Kang, Q.; Wu, Y.; Zhang, J.; Wang, J.; Tao, D.; Zhang, Q.; Cao, G. Dual Effects of Metal and Organic Ions Co-Intercalation Boosting the Kinetics and Stability of Hydrated Vanadate Cathodes for Aqueous Zinc-Ion Batteries. *Adv. Energy Mater.* **2023**, *13*, No. 2301480.
(30) Zhang, F.; Sun, X.; Du, M.; Zhang, X.; Dong, W.; Sang, Y.; Wang, J.; Li, Y.; Liu, H.; Wang, S. Weaker Interactions in Zn^{2+} and Organic Ion-Pre-Intercalated Vanadium Oxide toward Highly

https://doi.org/10.1021/acsenergylett.4c02709
ACS Energy Lett. 2024, 9, 5492−5501

Reversible Zinc-Ion Batteries. *Energy Environ. Mater.* **2021**, *4*, 620−630.
(31) Evans, H.; Post, J.; Ross, D.; Nelen, J. The Crystal Structure and Crystal Chemistry of Fernandinite and Corvusite. *Can. Mineral.* **1994**, *32*, 339−351.
(32) Liu, H.; Hou, X.; Fang, T.; Zhang, Q.; Gong, N.; Peng, W.; Li, Y.; Zhang, F.; Fan, X. Boosting Zinc-Ion Storage in Hydrated Vanadium Oxides Via Migration Regulation. *Energy Storage Mater.* **2023**, *55*, 279−288.
(33) Bondarenka, V.; Grebinskij, S.; Kaciulis, S.; Mattogno, G.; Mickevicius, S.; Tvardauskas, H.; Volkov, V.; Zakharova, G. Xps Study of Vanadium−Yttrium Hydrates. *J. Electron Spectrosc. Relat. Phenom.* **2001**, *120*, 131−135.
(34) Zhao, M.; Cao, Y.; Liu, X.; Deng, J.; Li, D.; Gu, H. Effect of Nitrogen Atomic Percentage on N^+-Bombarded MWCNTs in Cytocompatibility and Hemocompatibility. *Nanoscale Res. Lett.* **2014**, *9*, 142.
(35) Yoo, H. D.; Liang, Y.; Dong, H.; Lin, J.; Wang, H.; Liu, Y.; Ma, L.; Wu, T.; Li, Y.; Ru, Q.; Jing, Y.; An, Q.; Zhou, W.; Guo, J.; Lu, J.; Pantelides, S. T.; Qian, X.; Yao, Y. Fast Kinetics of Magnesium Monochloride Cations in Interlayer-Expanded Titanium Disulfide for Magnesium Rechargeable Batteries. *Nat. Commun.* **2017**, *8*, 339.
(36) Roessler, M. M.; Salvadori, E. Principles and Applications of EPR Spectroscopy in the Chemical Sciences. *Chem. Soc. Rev.* **2018**, *47*, 2534−2553.
(37) Wang, J.; Wang, J.; Jiang, Y.; Xiong, F.; Tan, S.; Qiao, F.; Chen, J.; An, Q.; Mai, L. $CaV_6O_{16}{\cdot}2.8H_2O$ with Ca^{2+} Pillar and Water Lubrication as a High-Rate and Long-Life Cathode Material for Ca-Ion Batteries. *Adv. Funct. Mater.* **2022**, *32*, No. 2113030.
(38) Chen, X.; Wang, P.; Feng, Z.; Meng, C.; Zhang, Y. Conductive Polymer Intercalated Vanadium Oxide on Carbon Cloth for Fast Ammonium-Ion Storage in Supercapacitor Applications. *Chem. Eng. J.* **2022**, *445*, No. 136747.
(39) Huang, H.; Xia, X.; Yun, J.; Huang, C.; Li, D.; Chen, B.; Yang, Z.; Zhang, W. Interfacial Engineering of Hydrated Vanadate to Promote the Fast and Highly Reversible H^+/Zn^{2+} Co-Insertion Processes for High-Performance Aqueous Rechargeable Batteries. *Energy Storage Mater.* **2022**, *52*, 473−484.
(40) Lv, T.; Zhu, G.; Dong, S.; Kong, Q.; Peng, Y.; Jiang, S.; Zhang, G.; Yang, Z.; Yang, S.; Dong, X.; Pang, H.; Zhang, Y. Co-Intercalation of Dual Charge Carriers in Metal-Ion-Confining Layered Vanadium Oxide Nanobelts for Aqueous Zinc-Ion Batteries. *Angew. Chem., Int. Ed.* **2023**, *62*, No. e202216089.
(41) Zhao, X.; Li, L.; Zheng, L.; Fan, L.; Yi, Y.; Zhang, G.; Han, C.; Li, B. 3*d*-Orbital Regulation of Transition Metal Intercalated Vanadate as Optimized Cathodes for Calcium-Ion Batteries. *Adv. Funct. Mater.* **2024**, *34*, No. 2309753.
(42) Ki Park, S.; Nakhanivej, P.; Seok Yeon, J.; Ho Shin, K.; Dose, W. M.; De Volder, M.; Bae Lee, J.; Jin Kim, H.; Park, H. S. Electrochemical and Structural Evolution of Structured V_2O_5 Microspheres During Li-Ion Intercalation. *J. Energy Chem.* **2021**, *55*, 108−113.
(43) Uchaker, E.; Zheng, Y. Z.; Li, S.; Candelaria, S. L.; Hu, S.; Cao, G. Z. Better Than Crystalline: Amorphous Vanadium Oxide for Sodium-Ion Batteries. *J. Mater. Chem. A* **2014**, *2*, 18208−18214.
(44) Wood, J. Ligand Field Theory. *Nature* **1970**, *226*, 1067−1068.
(45) Abbate, M.; Pen, H.; Czyżyk, M. T.; Groot, F. M. F. d.; Fuggle, J. C.; Ma, Y. J.; Chen, C. T.; Sette, F.; Fujimori, A.; Ueda, Y.; Kosuge, K. Soft X-Ray Absorption Spectroscopy of Vanadium Oxides. *J. Electron Spectrosc. Redat. Phenom.* **1993**, *62*, 185−195.
(46) Zhu, K.; Zhu, Q.; Jiang, M.; Zhang, Y.; Shao, Z.; Geng, Z.; Wang, X.; Zeng, H.; Wu, X.; Zhang, W.; Huang, K.; Feng, S. Modulating Ti t_{2g} Orbital Occupancy in a Cu/TiO_2 Composite for Selective Photocatalytic CO_2 Reduction to CO. *Angew. Chem., Int. Ed.* **2022**, *61*, No. e202207600.
(47) de Groot, F. M. F.; Fuggle, J. C.; Thole, B. T.; Sawatzky, G. A. 2p X-Ray Absorption of 3d Transition-Metal Compounds: An Atomic Multiplet Description Including the Crystal Field. *Phys. Rev. B* **1990**, *42*, 5459−5468.
(48) Wang, D.; Jiao, Y.; Shi, W.; Pu, B.; Ning, F.; Yi, J.; Ren, Y.; Yu, J.; Li, Y.; Wang, H.; Li, B.; Li, Y.; Nan, C.; Chen, L.; Shi, S. Fundamentals and Advances of Ligand Field Theory in Understanding Structure-Electrochemical Property Relationship of Intercalation-Type Electrode Materials for Rechargeable Batteries. *Prog. Mater. Sci.* **2023**, *133*, No. 101055.
(49) Assat, G.; Tarascon, J. M. Fundamental Understanding and Practical Challenges of Anionic Redox Activity in Li-Ion Batteries. *Nat. Energy* **2018**, *3*, 373−386.
(50) Chen, C.; Dong, C.; Ho, Y.; Chang, C.; Wei, D.; Chan, T.; Chen, J.; Jang, W.; Hsu, C.; Kumar, K.; Wu, M. Electronic and Atomic Structures of Gasochromic V_2O_5 Films. *EPL* **2013**, *101*, 17006.
(51) Alkorta, I.; Rozas, I.; Elguero, J. Bond Length-Electron Density Relationships: From Covalent Bonds to Hydrogen Bond Interactions. *Struct. Chem.* **1998**, *9*, 243−247.
(52) Liu, C.; Neale, Z. G.; Cao, G. Understanding Electrochemical Potentials of Cathode Materials in Rechargeable Batteries. *Mater. Today* **2016**, *19*, 109−123.
(53) Sawatzky, G. A.; Post, D. X-Ray Photoelectron and Auger Spectroscopy Study of Some Vanadium Oxides. *Phys. Rev. B* **1979**, *20*, 1546−1555.
(54) Lee, S.; Zajac, G. W.; Goodman, D. W. A Study of the Electronic Structure and Reactivity of $V/TiO_2(110)$ with Metastable Impact Electron Spectroscopy (MIES) and Ultraviolet Photoelectron Spectroscopy (UPS). *Top. Catal.* **2006**, *38*, 127−132.
(55) Whitten, J. E. Ultraviolet Photoelectron Spectroscopy: Practical Aspects and Best Practices. *Appl. Surf. Sci. Adv.* **2023**, *13*, No. 100384.
(56) Bermudez, V. M.; Williams, R. T.; Long, J. P.; Reed, R. K.; Klein, P. H. Photoemission Study of Hydrogen Adsorption on Vanadium Dioxide near the Semiconductor-Metal Phase Transition. *Phys. Rev. B* **1992**, *45*, 9266−9271.
(57) Zhang, P.; Gong, Y.; Fan, S.; Luo, Z.; Hu, J.; Peng, C.; Zhang, Q.; Li, Y.; Ren, X. Glutamic Acid Induced Proton Substitution of Sodium Vanadate Cathode Promotes High Performance in Aqueous Zinc-Ion Batteries. *Adv. Energy Mater.* **2024**, *14*, No. 2401493.
(58) Lazanas, A.; Prodromidis, M. Electrochemical Impedance Spectroscopy-a Tutorial. *ACS Meas. Sci. Au* **2023**, *3*, 162−193.
(59) Huang, J. Diffusion Impedance of Electroactive Materials, Electrolytic Solutions and Porous Electrodes: Warburg Impedance and Beyond. *Electrochim. Acta* **2018**, *281*, 170−188.
(60) Zhang, F.; Kang, Y.; Zhao, X.; Li, H.; Dong, H.; Wei, W.; Sang, Y.; Liu, H.; Wang, S. Boosting Charge Carrier Transport by Layer-Stacked $Mn_xV_2O_6/V_2C$ Heterostructures for Wide-Temperature Zinc-Ion Batteries. *Adv. Funct. Mater.* **2024**, *34*, No. 2402071.
(61) Liang, X.; Yan, L.; Li, W.; Bai, Y.; Zhu, C.; Qiang, Y.; Xiong, B.; Xiang, B.; Zou, X. Flexible High-Energy and Stable Rechargeable Vanadium-Zinc Battery Based on Oxygen Defect Modulated V_2O_5 Cathode. *Nano Energy* **2021**, *87*, No. 106164.
(62) Ding, J.; Du, Z.; Gu, L.; Li, B.; Wang, L.; Wang, S.; Gong, Y.; Yang, S. Ultrafast Zn^{2+} Intercalation and Deintercalation in Vanadium Dioxide. *Adv. Mater.* **2018**, *30*, No. 1800762.
(63) Hu, P.; Zhu, T.; Wang, X.; Wei, X.; Yan, M.; Li, J.; Luo, W.; Yang, W.; Zhang, W.; Zhou, L.; Zhou, Z.; Mai, L. Highly Durable $Na_2V_6O_{16}{\cdot}1.63H_2O$ Nanowire Cathode for Aqueous Zinc-Ion Battery. *Nano Lett.* **2018**, *18*, 1758−1763.
(64) Cai, P.; Wang, K.; He, X.; Li, Q.; Zhang, Z.; Li, M.; Li, H.; Zhou, M.; Wang, W.; Jiang, K. Electric-Field Harmony in V_2C/V_2O_5 Heterointerfaces toward High-Performance Aqueous Zn-Ion Batteries. *Energy Storage Mater.* **2023**, *60*, No. 102835.
(65) Cao, J.; Zhang, D.; Yue, Y.; Wang, X.; Pakornchote, T.; Bovornratanaraks, T.; Zhang, X.; Wu, Z. S.; Qin, J. Oxygen Defect Enriched $(NH_4)_2V_{10}O_{25}{\cdot}8H_2O$ Nanosheets for Superior Aqueous Zinc-Ion Batteries. *Nano Energy* **2021**, *84*, No. 105876.

https://doi.org/10.1021/acsenergylett.4c02709
ACS Energy Lett. 2024, 9, 5492−5501